



Modeling, Fabrication, and Electrical Testing of Metal-Insulator-Metal Diode

**by Dr. Terrance O'Regan, Matthew Chin, Cheng Tan,
and Dr. Anthony Birdwell**

ARL-TN-0464

December 2011

NOTICES

Disclaimers

The findings in this report are not to be construed as an official Department of the Army position unless so designated by other authorized documents.

Citation of manufacturer's or trade names does not constitute an official endorsement or approval of the use thereof.

Destroy this report when it is no longer needed. Do not return it to the originator.

Army Research Laboratory

Adelphi, MD 20783-1197

ARL-TN-0464

December 2011

Modeling, Fabrication, and Electrical Testing of Metal-Insulator-Metal Diode

**Dr. Terrance O'Regan, Matthew Chin, Cheng Tan,
and Dr. Anthony Birdwell
Sensors and Electron Devices Directorate, ARL**

REPORT DOCUMENTATION PAGE

Form Approved
OMB No. 0704-0188

Public reporting burden for this collection of information is estimated to average 1 hour per response, including the time for reviewing instructions, searching existing data sources, gathering and maintaining the data needed, and completing and reviewing the collection information. Send comments regarding this burden estimate or any other aspect of this collection of information, including suggestions for reducing the burden, to Department of Defense, Washington Headquarters Services, Directorate for Information Operations and Reports (0704-0188), 1215 Jefferson Davis Highway, Suite 1204, Arlington, VA 22202-4302. Respondents should be aware that notwithstanding any other provision of law, no person shall be subject to any penalty for failing to comply with a collection of information if it does not display a currently valid OMB control number.

PLEASE DO NOT RETURN YOUR FORM TO THE ABOVE ADDRESS.

1. REPORT DATE (DD-MM-YYYY) December 2011		2. REPORT TYPE Final		3. DATES COVERED (From - To) October 2010 to September 2011	
4. TITLE AND SUBTITLE Modeling, Fabrication, and Electrical Testing of Metal-Insulator-Metal Diode				5a. CONTRACT NUMBER	
				5b. GRANT NUMBER	
				5c. PROGRAM ELEMENT NUMBER	
6. AUTHOR(S) Dr. Terrance O'Regan, Matthew Chin, Cheng Tan, and Dr. Anthony Birdwell				5d. PROJECT NUMBER T0-SE-11-01	
				5e. TASK NUMBER	
				5f. WORK UNIT NUMBER	
7. PERFORMING ORGANIZATION NAME(S) AND ADDRESS(ES) U.S. Army Research Laboratory ATTN: RDRL-SER-E 2800 Powder Mill Road Adelphi, MD 20783-1197				8. PERFORMING ORGANIZATION REPORT NUMBER ARL-TN-0464	
9. SPONSORING/MONITORING AGENCY NAME(S) AND ADDRESS(ES)				10. SPONSOR/MONITOR'S ACRONYM(S)	
				11. SPONSOR/MONITOR'S REPORT NUMBER(S)	
12. DISTRIBUTION/AVAILABILITY STATEMENT Approved for public release; distribution unlimited.					
13. SUPPLEMENTARY NOTES					
14. ABSTRACT We fabricated, tested, and modeled metal-insulator-metal (MIM) diodes for application into a nanorectenna energy-harvesting system. The MIM diodes were constructed of a niobium (Nb) bottom metal, niobium pentoxide (Nb ₂ O ₅) dielectric, and varying top metals (copper, silver, and gold). Modeling and electrical testing were used to extract the dielectric constant of Nb ₂ O ₅ as well as the metal-insulator barrier heights. The modeling also gave insight into the so-called "rectification reversal," where the rectification polarity depends on which transport mechanism (thermionic emission or tunneling) dominates. Including an approximation for the image potential in the model was shown to be critically important in understanding the rectification reversal and quantitatively reproducing the measured electrical data. Future work will focus on verifying extracted barrier heights by photoemission techniques and exploring other material stacks. In addition, the dielectric thickness will be reduced and the temperature varied to further study tunneling dominated rectification.					
15. SUBJECT TERMS Metal-Insulator-Metal diode, terahertz rectification, tunneling, thermionic, barrier height					
16. SECURITY CLASSIFICATION OF:			17. LIMITATION OF ABSTRACT UU	18. NUMBER OF PAGES 26	19a. NAME OF RESPONSIBLE PERSON Dr. Terrance O'Regan
a. REPORT Unclassified	b. ABSTRACT Unclassified	c. THIS PAGE Unclassified			19b. TELEPHONE NUMBER (Include area code) (301) 394-1868

Contents

1. Introduction	1
2. MIM Model	1
2.1 Potential Energy and Image Potential	1
2.2 Thermionic Emission-limited Current	3
2.3 Tunneling-limited Current	5
3. MIM Diode Fabrication	9
4. Comparison to Experimental Measurements	11
5. Conclusions and Future Work	15
References	17
Distribution	18

List of Figures

1	Potential energy at 1-V forward bias for a symmetric MIM diode with $\varphi_1 = 1$ eV, $\varphi_2 = 1$ eV, $s = 10$ nm, $K = 4$, $m = m_0$, and $T = 300$ K	3
2	Total potential energy with varying dielectric constant, K , values for the symmetric MIM diode in figure 1	3
3	Maximum energy barrier above the negatively biased Fermi level for the forward biased MIM diode in figure 1	4
4	Thermionic emission-limited current through the symmetric MIM diode in figure 1	5
5	Potential energy at 1-V forward bias for a symmetric MIM diode with $\varphi_1 = 1$ eV, $\varphi_2 = 1$ eV, $s = 5$ nm, $K = 4$, $m = m_0$, and $T = 300$ K	6
6	Maximum and average barrier height vs. applied bias for the symmetric MIM diode in figure 5	7
7	Absolute value of tunnel-limited, thermal emission-limited, and total currents vs. applied bias for the symmetric MIM diode in figure 5	7
8	Absolute value of tunnel-limited, thermal emission-limited, and total currents vs. applied bias for an asymmetric MIM diode with $\varphi_1 = 0.2$ eV, $\varphi_2 = 1.2$ eV, $s = 5$ nm, $K = 4$, $m = m_0$, and $T = 300$ K	8
9	Absolute value of tunnel-limited, thermal emission-limited, and total currents vs. applied bias for an asymmetric MIM diode with $\varphi_1 = 0.2$ eV, $\varphi_2 = 2.2$ eV, $s = 5$ nm, $K = 4$, $m = m_0$, and $T = 300$ K	9
10	Maximum barrier height and tunneling distance vs. applied bias for the asymmetric MIM diode in figure 9	9
11	Simple square pillar structures were used as MIM diodes based on niobium (Nb)/niobium pentoxide (Nb ₂ O ₅)/x material stacks, where x designates copper (Cu), silver (Ag), and gold (Au) for different device sets. The square pillars had dimensions of $60 \mu\text{m} \times 60 \mu\text{m}$, and were drawn in AutoCAD	10
12	The image shown is an example of MIM diodes fabricated using the process described in this section	12

13	In this cartoon, a top and cut-away view of the MIM tunnel diodes fabricated are provided with the material stack thicknesses and dimensions of the pillar structure	13
14	Modeled and experimental current characteristics for an Nb/Nb ₂ O ₅ /Cu device	13
15	Modeled and experimental current characteristics for an Nb/Nb ₂ O ₅ /Ag device	14
16	Modeled and experimental current characteristics for an Nb/Nb ₂ O ₅ /Au device	14

List of Tables

1	Best-fit MIM modeling parameters	15
---	--	----

INTENTIONALLY LEFT BLANK

1. Introduction

Metal-insulator-metal (MIM) diodes that rely on quantum-mechanical tunneling for current generation are one of the few structures capable of rectifying radiation absorbed by a nano-antenna designed for the terahertz frequency range (visible and infrared wavelengths) (1, 2). For this application, diodes with current-voltage (I-V) characteristics that show high asymmetry, strong nonlinearity, fast responsivity, low hysteresis, and low turn-on voltage are desired (3). We show that these properties depend primarily upon the materials that make up the MIM stack.

We model the tunneling and thermionic currents, and compare to experimental data measured on MIM diodes that we fabricated. Our model gives insight into the quality and variability of the fabricated MIM structures. The model confirms that the MIM diode must be dominated by quantum mechanical tunneling and be strongly asymmetric to rectify terahertz radiation. We use our model to investigate the design space that meets these requirements.

The outline of this report is as follows. First, we discuss the potential energy, an approximation for the image potential, and the total potential energy. We show how the image potential lowers the total potential barrier and its dependence on dielectric constant of the insulator. Then, we discuss the thermionic emission-limited current as a function of *maximum* barrier height and temperature. Next, we explain tunneling limited current and its dependence on *average* barrier height and tunneling distance, and explore thermionic emission and tunneling current as a function of insulator thickness and metal-insulator barrier heights. Finally, we describe the MIM fabrication process and compare our model to experimental data.

2. MIM Model

2.1 Potential Energy and Image Potential

The magnitude of the intrinsic electric field between two electrodes separated by an insulating film is

$$F_i = \frac{(\Phi_{m1} - \Phi_{m2})}{es}, \quad (1)$$

where Φ_{m1} and Φ_{m2} are the metal workfunctions, s is the insulator thickness, and e is the unit of electron charge. The barrier heights at the metal-insulator interfaces are related as

$$\varphi_2 = \varphi_1 + eF_i s, \quad (2)$$

where φ_1 and φ_2 are the metal-insulator barrier heights. It is straightforward to show that the potential energy between the electrodes can be then written as

$$\varphi(x) = \varphi_1 + \Delta\Phi(x/s), \quad (3)$$

where $\Delta\Phi = \Phi_{m1} - \Phi_{m2}$ and x is the position coordinate where we have defined the diode to be oriented along the x -axis. If we assume that electrode-1 is grounded, and a voltage is applied to electrode-2, the potential energy between the electrodes is now

$$\varphi(x) = \varphi_1 + (\Delta\Phi - eV)(x/s), \quad (4)$$

where V is the applied bias. To find the barrier height between an arbitrary metal and insulator, we need the workfunction of the metal, Φ_m , and the electron affinity of the insulator, χ_{ins} . The barrier height then follows as

$$\varphi = \Phi_m - \chi_{\text{ins}}. \quad (5)$$

We show later that the barrier heights are critical in determining the current through an MIM diode.

The image potential between two electrodes separated by an insulator can be approximated as (4, 5)

$$V_{\text{im}}(x) = \frac{-0.288s}{Kx(s-x)}, \quad (6)$$

where s and x are in units of nm, and K is the high-frequency dielectric constant of the insulator.

The total potential energy in the insulator is then

$$V_{\text{tot}} = \varphi(x) + V_{\text{im}}(x), \quad (7)$$

or more explicitly

$$V_{\text{tot}} = \varphi_1 + (\Delta\Phi - eV)(x/s) + \frac{-0.288s}{Kx(s-x)}. \quad (8)$$

Figure 1 shows the potential energy, image potential, and total potential energy for a symmetric diode with $\varphi_1 = \varphi_2 = 1$ eV, $s = 10$ nm, $K = 4$, and $V = 1$ V. If we denote the Fermi levels in electrode-1 and electrode-2 as E_{F1} and E_{F2} , respectively, the applied bias is $E_{F1} - E_{F2}$. The image potential is negative and reduces the total maximum potential barrier. The image potential also smooths out the abrupt corners of the potential energy.

Figure 2 shows the potential energy and total potential energy for the same symmetric diode as in figure 1 but for varying values of K . As K increases, the area under the potential energy barrier increases and the potential energy barrier tends towards φ . Thus, for insulators with smaller dielectric constants, the peak barrier and average barrier heights decrease, which we show later increases the thermal emission and tunnel currents.

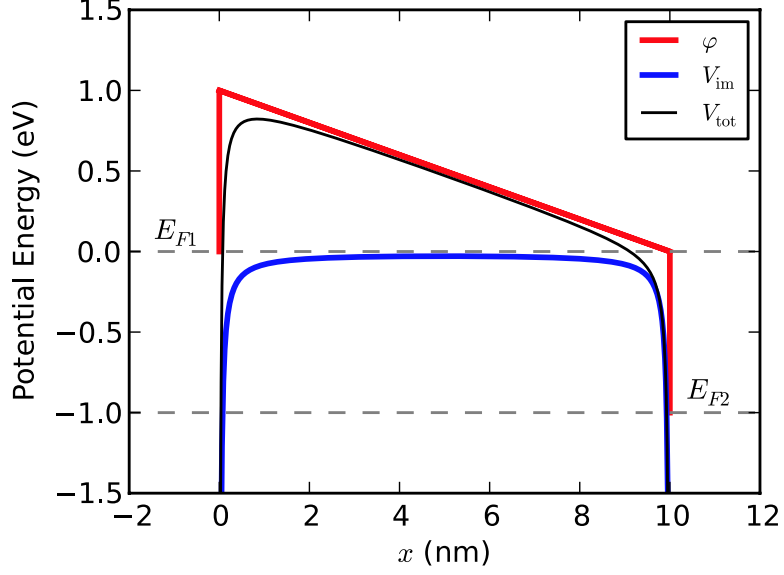


Figure 1. Potential energy at 1-V forward bias for a symmetric MIM diode with $\varphi_1 = 1$ eV, $\varphi_2 = 1$ eV, $s = 10$ nm, $K = 4$, $m = m_0$, and $T = 300$ K.

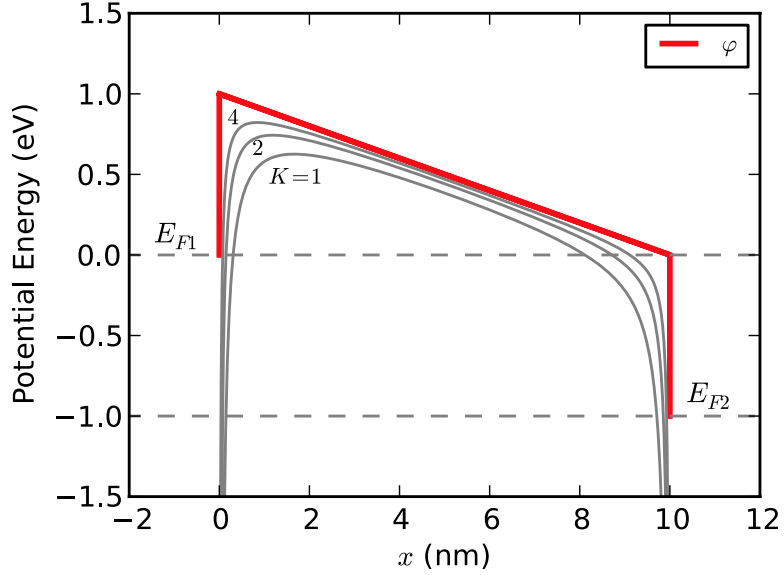


Figure 2. Total potential energy with varying dielectric constant, K , values for the symmetric MIM diode in figure 1.

2.2 Thermionic Emission-limited Current

The thermionic emission-limited current through an MIM diode is (5)

$$J = A_{\text{th}} T^2 e^{-\varphi_1'/k_B T} (1 - e^{-eV/k_B T}), \quad (9)$$

where φ'_1 is the maximum barrier height above the negatively biased electrode, T is the temperature, and

$$A_{\text{th}} = 4\pi m e k_B^2 / h^3, \quad (10)$$

where m is the electron mass (set to m_o throughout this report), k_B is Boltzmann's constant, and h is Plank's constant.

From equation 9, we see that the thermionic emission-limited current is exponentially dependent on φ'_1 (always referenced to the Fermi level of the negatively biased electrode). From figure 3, we see that φ'_1 is constant (set by $\Phi_m - \chi_{\text{ins}}$) when neglecting the image potential. However, when including the image potential, φ'_1 decreases with increasing bias. In fact, at 1-V forward bias, φ'_1 is nearly 0.2 eV below the no image potential case. Figure 4 shows the calculated thermionic emission-limited current through a symmetric MIM diode described in figure 1 with and without the image potential included. The conclusion here is that the image potential must be included if one hopes to accurately model the thermionic emission limited current through an MIM diode.

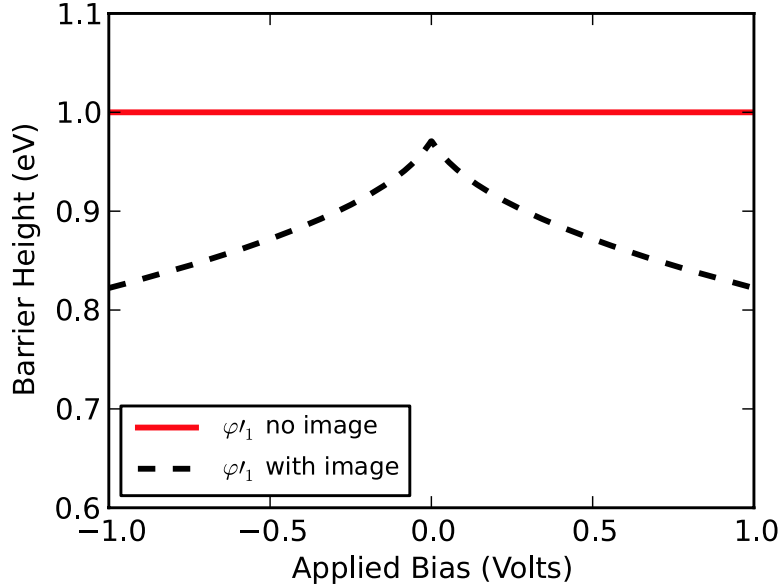


Figure 3. Maximum energy barrier above the negatively biased Fermi level for the forward biased MIM diode in figure 1.

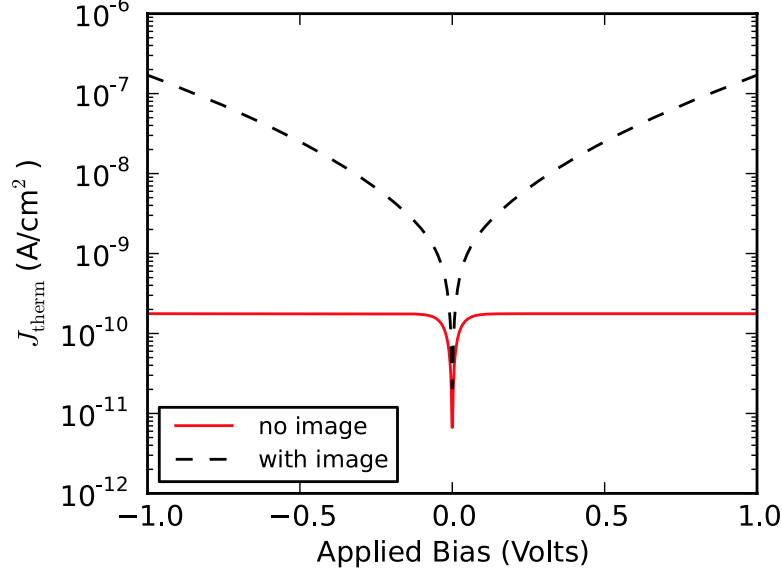


Figure 4. Thermionic emission-limited current through the symmetric MIM diode in figure 1.

2.3 Tunneling-limited Current

The tunnel-limited current through an MIM diode is (4)

$$J = J_0 \left\{ \bar{\varphi} \exp \left(-A_{\text{tun}} \bar{\varphi}^{\frac{1}{2}} \right) - (\bar{\varphi} + eV) \exp \left[-A_{\text{tun}} (\bar{\varphi} + eV)^{\frac{1}{2}} \right] \right\}, \quad (11)$$

where

$$J_0 = \frac{e}{2\pi h (\beta \Delta s)^2}, \quad (12)$$

and the mean barrier height, $\bar{\varphi}$, above the Fermi level of the negatively biased electrode is

$$\bar{\varphi} = \frac{1}{\Delta s} \int_{s_1}^{s_2} \varphi(x) dx, \quad (13)$$

where s_1 and s_2 are the positions where the potential energy barrier intersects the Fermi level of the negatively biased electrode and $\Delta s = s_2 - s_1$ is the tunneling distance. The A_{tun} factor is

$$A_{\text{tun}} = (4\pi\beta\Delta s/h) (2m)^{\frac{1}{2}}, \quad (14)$$

where β is a correction factor given in the appendix of reference 4 (we have set $\beta = 1$ in this report).

In figure 4, thermionic emission-limited current dominates for $s = 10$ nm. Now let us explore a symmetric MIM diode with the same parameters as figure 1 but with $s = 5$ nm.

Figure 5 shows the potential energy and total potential energy with the image potential included. Compared to figure 1 ($s = 15$ nm), the total potential barrier is significantly reduced. Figure 6 shows that the maximum potential barrier height is higher than the average potential barrier height for each applied bias. Comparing figure 6 to figure 2, we see that the maximum barrier height is reduced as s is reduced due to the larger contribution of the image potential. Figure 7 shows the absolute value of tunnel-limited, thermal-emission limited, and total current versus applied bias. At low bias, the thermal emission-limited current dominates. The tunneling-limited current increases rapidly with bias and crosses over the thermal current at higher bias.

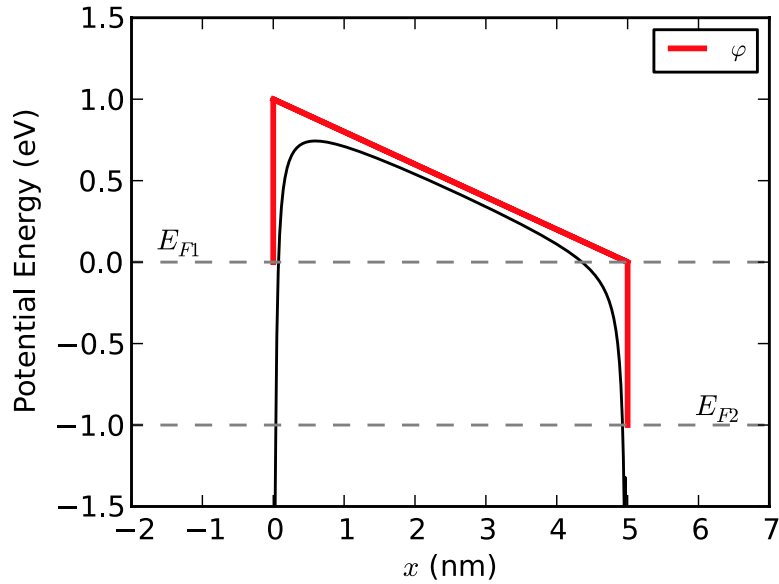


Figure 5. Potential energy at 1-V forward bias for a symmetric MIM diode with $\varphi_1 = 1$ eV, $\varphi_2 = 1$ eV, $s = 5$ nm, $K = 4$, $m = m_0$, and $T = 300$ K.

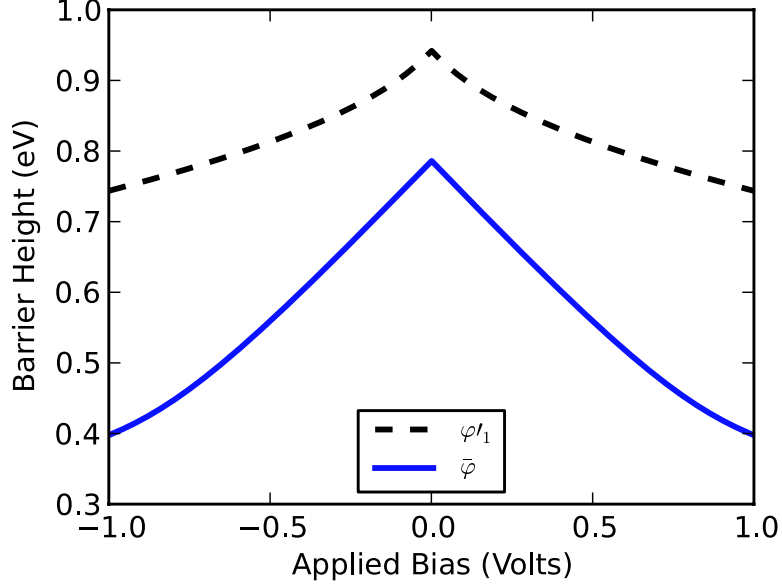


Figure 6. Maximum and average barrier height vs. applied bias for the symmetric MIM diode in figure 5.

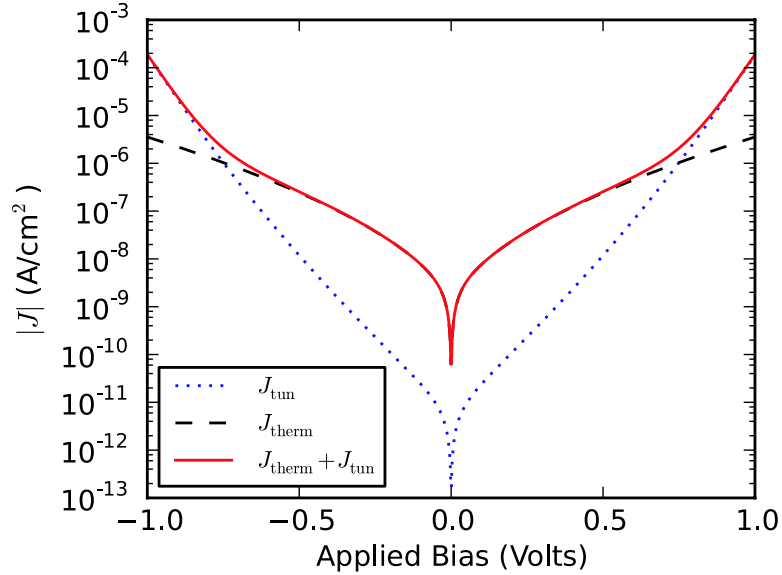


Figure 7. Absolute value of tunnel-limited, thermal emission-limited, and total currents vs. applied bias for the symmetric MIM diode in figure 5.

Next we consider a highly asymmetric diode with one nearly ohmic metal-insulator junction. In this case, we assume $\varphi_1 = 0.2$ eV, $\varphi_2 = 1.2$ eV, $s = 5$ nm, $K = 4$, and $T = 300$ K. Figure 8 shows the absolute value of the current-density components. There are three important characteristics in figure 8 that are important. First, the tunneling current is not nearly as asymmetric as the thermal current; second, the tunnel current dominates the thermal current for all negative voltages but only for small positive voltages;

and third, the tunneling-limited current acts as a diode in the reverse polarity compared to the thermal-limited current. This second point may not pose a problem, as the diode will function at lower AC (terahertz) bias. However, the tunnel current must be made more asymmetric for the MIM structure to act as a diode. The third point, sometimes referred to as “rectification reversal” is due to the switching between Fowler-Nordheim and direct tunneling. Rectification reversal can be explained by figure 10, where the average barrier height and tunneling distance have offset each other, which leads to a reversed polarity rectification, and in general, a more symmetric I-V characteristic. Figure 9 show the current density for the same parameters in figure 8, but with $\varphi_2 = 2.2$ eV. In this case, the tunneling-limited current clearly dominates (thermal current is not shown), but the I-V characteristic is still quite symmetric.

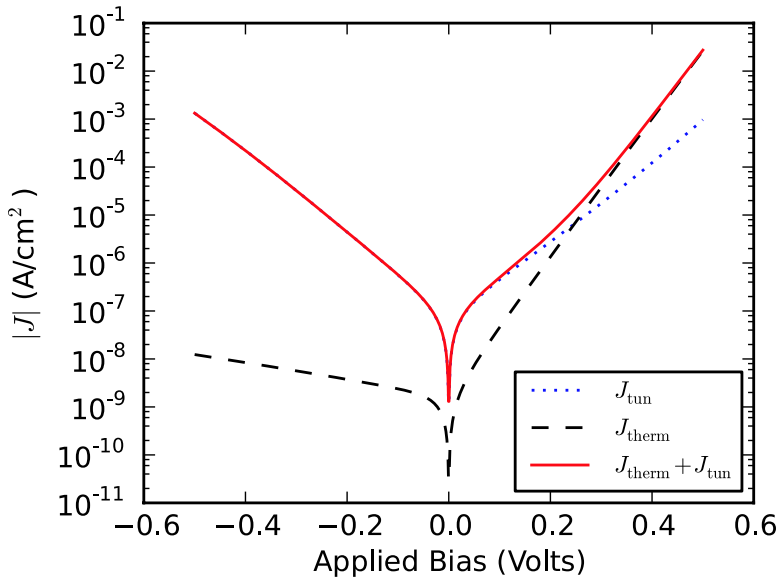


Figure 8. Absolute value of tunnel-limited, thermal emission-limited, and total currents vs. applied bias for an asymmetric MIM diode with $\varphi_1 = 0.2$ eV, $\varphi_2 = 1.2$ eV, $s = 5$ nm, $K = 4$, $m = m_0$, and $T = 300$ K.

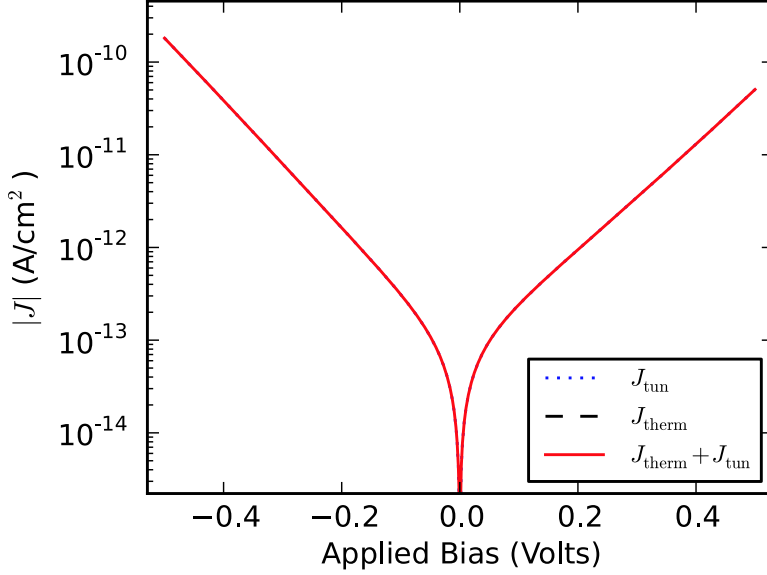


Figure 9. Absolute value of tunnel-limited, thermal emission-limited, and total currents vs. applied bias for an asymmetric MIM diode with $\varphi_1 = 0.2$ eV, $\varphi_2 = 2.2$ eV, $s = 5$ nm, $K = 4$, $m = m_0$, and $T = 300$ K.

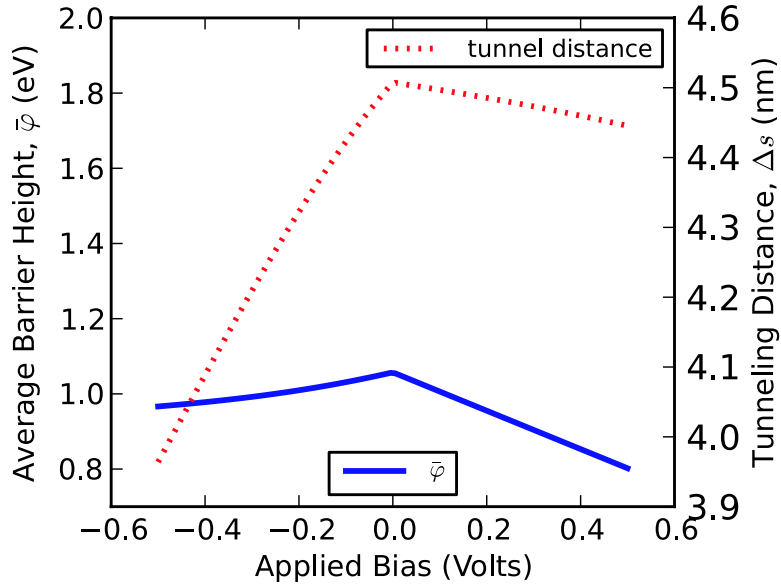


Figure 10. Maximum barrier height and tunneling distance vs. applied bias for the asymmetric MIM diode in figure 9.

3. MIM Diode Fabrication

MIM diodes were designed and fabricated for the purpose of validating the model discussed in the previous sections. Simple column structures composed of a blanket bottom metal layer, blanket insulator layer, and a square-patterned top metal layer were chosen due to

their ease of fabrication. An image of the photolithographic mask design for the column structures is shown in figure 11.

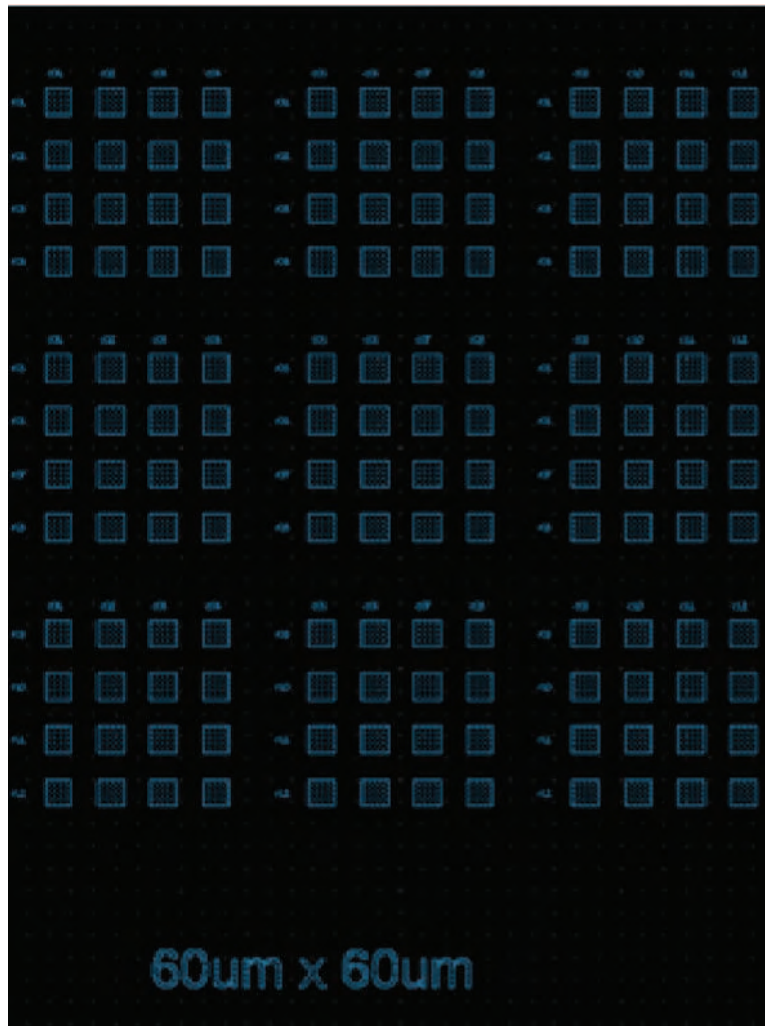


Figure 11. Simple square pillar structures were used as MIM diodes based on niobium (Nb)/niobium pentoxide (Nb_2O_5)/x material stacks, where x designates copper (Cu), silver (Ag), and gold (Au) for different device sets. The square pillars had dimensions of $60 \mu\text{m} \times 60 \mu\text{m}$, and were drawn in AutoCAD.

The Nb/ Nb_2O_5 material system was chosen due to this combination's reported low barrier height (6, 7), which provides a low turn-on voltage in a MIM diode. Previously reported measurements have specified the barrier height of the Nb/ Nb_2O_5 junction to be between 133 to 300 meV (6, 7). The top metals were chosen for their relatively high work function difference with respect to Nb. A high work function difference between the two metal layers is considered the primary mechanism for high asymmetry and large nonlinearity in MIM diode I-V characteristics (3, 8). It has already been reported that Cu, Ag, and Au have relatively good asymmetric I-V characteristics when acting as the second metal layer in a Nb/ Nb_2O_5 /x MIM diode, where x represents one of the three metals listed (7).

A blanket 80-nm-thick Nb metal film was deposited via a room-temperature sputter process on top of a 500- μm -thick silicon (Si) substrate. Next, 15-nm of Nb_2O_5 was grown via an electrochemical (anodic) oxidation process on top of the Nb metal film, with approximately 5 nm of native Nb_2O_5 already present due to the exposure to ambient air after the Nb film deposition. The surface roughness of the as-deposited Nb film was measured to be 0.9 nm (average, root mean square [RMS]); and after the Nb_2O_5 films were electrochemically grown, the surface roughness was measured to be 1.1 nm (average, RMS). The Nb_2O_5 thin films were provided by collaborators at the National Renewable Energy Laboratory (NREL) in Golden, CO. A WITec Alpha 300 A atomic force microscope (AFM) was used to characterize the surface roughness of the Nb and Nb_2O_5 layers (measurements performed at NREL). The thickness of the Nb metal film was determined via profilometry, while the thickness of the Nb_2O_5 film was determined using ellipsometry, transmission electron microscopy (TEM) cross-sections, and x-ray reflectivity.

The top metals were photolithographically patterned using a lift-off process. For model validation purposes, the Au, Cu, and Ag top metals were deposited on separate sample sets. The geometric structures were photo-patterned using the AZ5214E photoresist and a Karl Suss MA6 photoaligner. Au and Ag were deposited using a CHA electron-beam evaporation system, with a deposition rate of 2 $\text{\AA}/\text{s}$. Cu was deposited using a Kurt Lesker PVD75 thermal evaporation system, with a deposition rate of 3 $\text{\AA}/\text{s}$. For each of the three top metals, approximately 1,600 \AA was deposited on top of the Nb_2O_5 layer. The thickness of the top metal films was determined through the use of profilometry. Figure 12 provides an example of an optical microscopic view (from the top) of a device set fabricated using the process described in this section, while figure 13 provides a cartoon image of a completed MIM diode stack.

4. Comparison to Experimental Measurements

The fabricated devices were measured with a Keithley 4200 Semiconductor Characterization System connected to a Desert Cryogenic Probestation. The experimental measurements were done at a temperature of 298 K and vacuum pressures below 1×10^{-4} torr. The electrical characterization involved a dual voltage sweep from -1 to 1 V and back in voltage steps of 1×10^{-2} V on the top electrode while holding the bottom electrode constant relative to ground. A 2.0-s hold time was used prior to the first current measurement on each sweep to allow devices to settle.

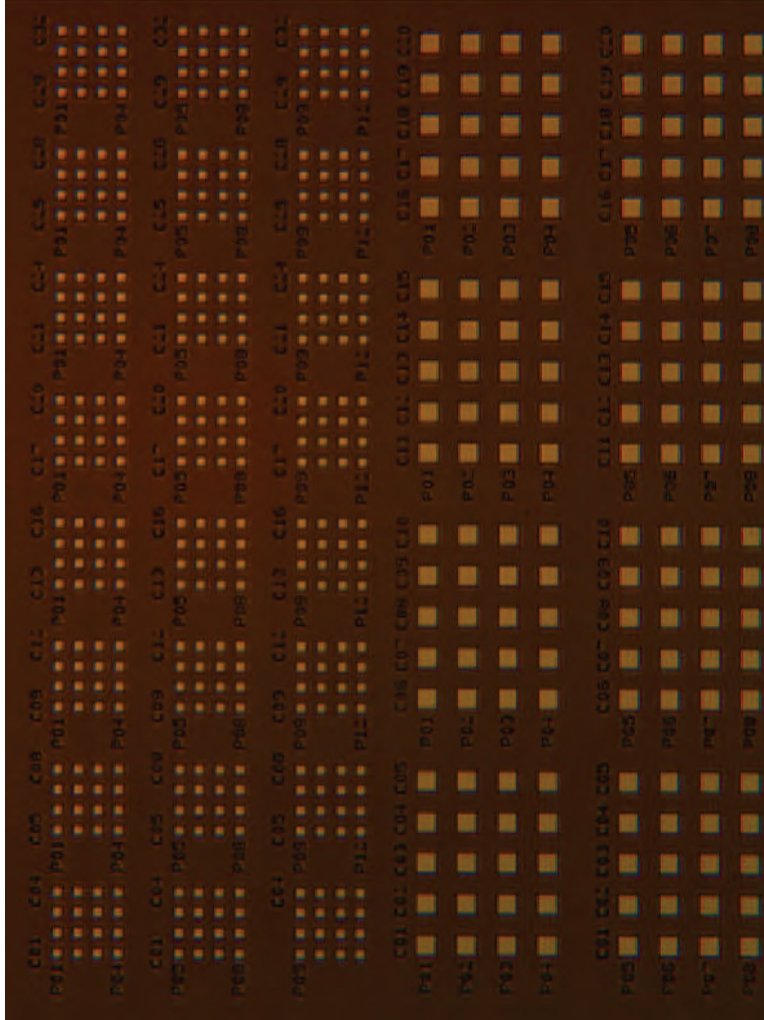


Figure 12. The image shown is an example of MIM diodes fabricated using the process described in this section.

The resulting current was then extracted and used for fitting. During the fitting process, parameters φ_1 and φ_2 were modified in order to produce a line of best fit. Parameters T and s were set to values of 298 K and 18 nm (to account for 15 nm of grown oxide and 5 nm of low-quality native oxide), respectively. On the other hand, K was experimentally determined for each individual I-V measurement from the slope of the $\ln \sigma$ vs. $E k_B * T$ graph assuming electrode-limited conduction, where σ is the conductivity and E is the electric field (9). If the value of K was experimentally determined to be less than 1, its value was set to 1 in the fitting process.

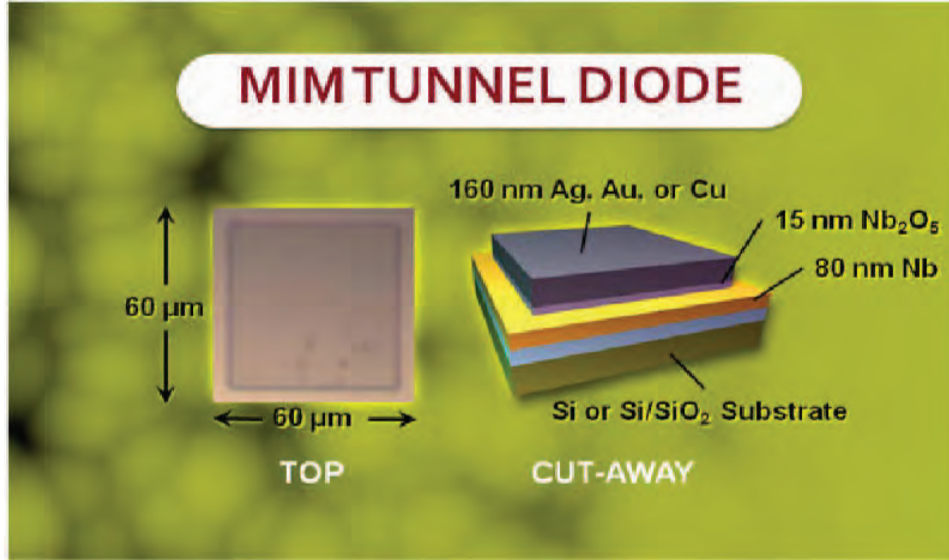


Figure 13. In this cartoon, a top and cut-away view of the MIM tunnel diodes fabricated are provided with the material stack thicknesses and dimensions of the pillar structure.

The results of the three different devices composed of Nb/Nb₂O₅/x, where x can be Cu, Ag, or Au are shown in figures 14, 15, and 16. The values of the modeling parameters used are given in table 1. Nb is the bottom electrode in all the experiments performed.

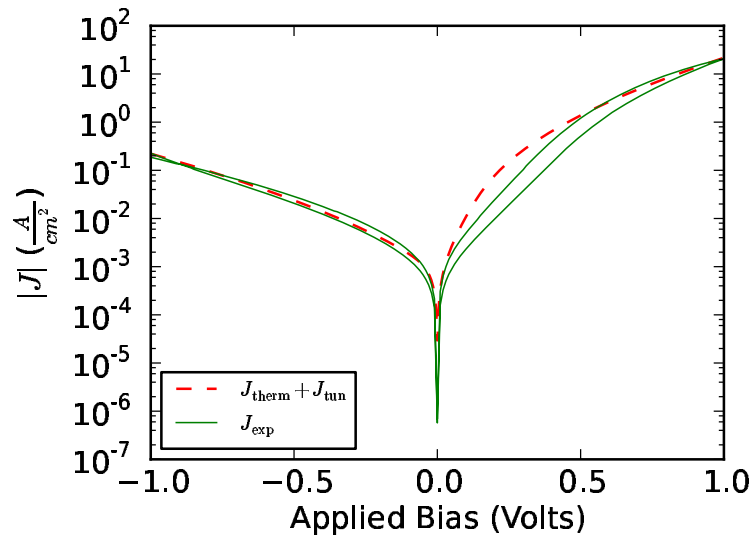


Figure 14. Modeled and experimental current characteristics for an Nb/Nb₂O₅/Cu device.

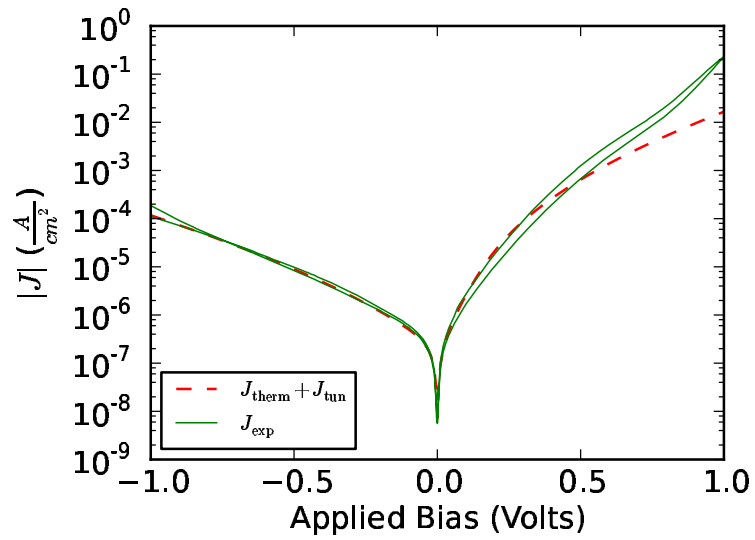


Figure 15. Modeled and experimental current characteristics for an Nb/Nb₂O₅/Ag device.

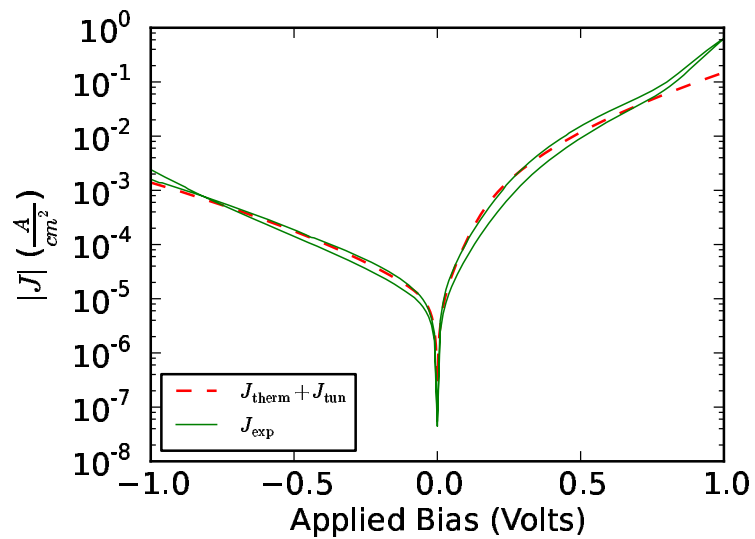


Figure 16. Modeled and experimental current characteristics for an Nb/Nb₂O₅/Au device.

Table 1. Best-fit MIM modeling parameters.

$M_1/I/M_2$	K	φ_1 (eV)	φ_2 (eV)
Nb/Nb ₂ O ₅ /Cu	1.36	0.55	0.7
Nb/Nb ₂ O ₅ /Ag	1.00	0.77	0.94
Nb/Nb ₂ O ₅ /Au	1.60	0.66	0.81

From the fitting, we can see that there are slight differences between the experiment and theoretical data, though the model gives a good match to the experimental behaviors in general. The differences are primarily detected in the positive bias response, which is mostly determined by the Nb/Nb₂O₅ barrier interface φ_1 . This suggests that there are parameters or non-idealities in the device unaccounted for by the modeling. Ideas for such non-idealities include trapped charges in the oxide and noise introduced from fabrication steps.

5. Conclusions and Future Work

In the present work, we fabricated MIM diodes, electrically tested them, and used modeling to extract high-frequency dielectric constants and metal-insulator barrier heights. In addition, the modeling gave insight into the design space necessary to produce asymmetric tunneling I-V characteristics. Specifically, thermionic current was shown to be limited by large barrier heights while tunneling current was shown to dominate when using thin (≈ 5 nm) dielectrics. We showed that the metal workfunctions must also be highly asymmetric in order to produce asymmetric I-V curves. Asymmetric I-V characteristics dominated by quantum-mechanical tunneling were shown to be difficult to achieve because of the rectification reversal effect.

In future work, we plan on verifying the electrically extracted barrier heights through alternative microanalysis techniques and by investigating other material systems. Surface photovoltage spectroscopy, photoemission, and thermal emission measurement methods will be used to confirm the logarithmic electrical-conductivity measurements collected in this report. The results from these methods will be inserted into the current model to increase accuracy and provide additional insight into the electrical properties of MIM diodes.

Additionally, future MIM diodes will be fabricated using thinner dielectric films with thicknesses ranging from 2 to 5 nm. This will allow us to investigate the contributions of both tunneling and thermionic emission. Low temperature and graded temperature measurements will provide insight to the contribution ratio between the two emission types in MIM diodes. Temperature measurements and calculations will provide the ability to

further extract metal-insulator barrier heights. Different metal contact combinations and other metals will be reviewed to determine possible material systems that provide even higher asymmetric MIM diode I-V characteristics than current MIM diode devices. Besides the Nb, Cu, Ag, and Au reviewed in this report, platinum (Pt), tantalum (Ta), nickel (Ni), and chromium (Cr) may also be investigated.

References

- [1] Hobbs, Philip C. D.; Laibowitz, Robert B.; Libsch, Frank R. Ni-NiO-Ni Tunnel Junctions for Terahertz and Infrared Detection. *Appl. Opt.* **November 2005**, *44* (32), 6813–6822.
- [2] Fumeaux, C.; Herrmann, W.; Kneubhl, F. K.; Rothuizen, H. Nanometer Thin-film Ni-NiO-Ni Diodes for Detection and Mixing of 30 THz Radiation. *Infrared Physics and Technology* **1998**, *39* (3), 123–183.
- [3] Berland, B. *Photovoltaic Technologies Beyond the Horizon: Optical Rectenna Solar Cell*; NREL/SR-520-33263; NREL, August 2011.
- [4] Simmons, J. G. Generalized Formula for the Electric Tunnel Effect between Similar Electrodes Separated by a Thin Insulating Film. *J. Appl. Phys.* **1963**, *34* (6), 1793–1803.
- [5] Simmons, J. G. Potential Barriers and Emission-limited Current Flow Between Closely Spaced Parallel Metal Electrodes. *J. Appl. Phys.* **1964**, *35* (8), 2472–2481.
- [6] Shirakashi, Jun-ichi; Matsumoto, Kazuhiko; Miura, Naruhisa; Konagai, Makoto. Nb/Nb Oxide-based Planar-type Metal/Insulator/Metal (MIM) Diodes Fabricated by Atomic Force Microscope (AFM) Nano-oxidation Process. *Japanese Journal of Applied Physics* **1997**, *36* (Part 2, No. 8B), L1120–L1122.
- [7] Periasamy, Prakash; Berry, Joseph J.; Dameron, Arrelaine A.; Bergeson, Jeremy D.; Ginley, David S.; O’Hayre, Ryan P.; Parilla, Philip A. Fabrication and Characterization of MIM Diodes Based on Nb/Nb₂O₅ Via a Rapid Screening Technique. *Advanced Materials* **2011**, *23* (27), 3080–3085.
- [8] Krishnan, S.; La Rosa, H.; Stefanakos, E.; Bhansali, S.; Buckle, K. Design and Development of Batch Fabricatable Metal-Insulator-Metal Diode and Microstrip Slot Antenna as Rectenna Elements. *Sensors and Actuators A: Physical* **2008**, *142* (1), 40–47.
- [9] Simmons, John G. Poole-Frenkel Effect and Schottky Effect in Metal-Insulator-Metal Systems. *Phys. Rev.* **March 1967**, *155*, 657–660.

NO. OF COPIES	ORGANIZATION
1 ELECT	ADMNSTR DEFNS TECHL INFO CTR ATTN DTIC OCP 8725 JOHN J KINGMAN RD STE 0944 FT BELVOIR VA 22060-6218
1 CD	OFC OF THE SECY OF DEFNS ATTN ODDRE (R&AT) THE PENTAGON WASHINGTON DC 20301-3080
1	US ARMY RSRCH DEV AND ENGRG CMND ARMAMENT RSRCH DEV & ENGRG CTR ARMAMENT ENGRG & TECHN LGY CTR ATTN AMSRD AAR AEF T J MATTS BLDG 305 ABERDEEN PROVING GROUND MD 21005-5001
1	US ARMY ARDEC ATTN AMSRD AAR AEE P C HAINES BLDG 25 PICATINNY ARSENAL NJ 07806-5000
1	US ARMY ARDEC ATTN AMSRD AAR AEM C A MARSTON BLDG 61S PICATINNY ARSENAL NJ 07806-5000
3	US ARMY ARDEC ATTN AMSRD AAR AEM L S GILMAN ATTN AMSRD AAR AEP F O NGUYEN ATTN AMSRD AAR AEP F S SHRI BLDG 65S PICATINNY ARSENAL NJ 07806-5000
1	US ARMY INFO SYS ENGRG CMND ATTN AMSEL IE TD A RIVERA FT HUACHUCA AZ 85613-5300
1	COMMANDER US ARMY RDECOM ATTN AMSRD AMR W C MCCORKLE 5400 FOWLER RD REDSTONE ARSENAL AL 35898-5000

NO. OF COPIES	ORGANIZATION
1	US GOVERNMENT PRINT OFF DEPOSITORY RECEIVING SECTION ATTN MAIL STOP IDAD J TATE 732 NORTH CAPITOL ST NW WASHINGTON DC 20402
18	US ARMY RSRCH LAB ATTN IMNE ALC HRR MAIL & RECORDS MGMT ATTN RDRL SER L O NAYFEH ATTN RDRL CIO LL TECHL LIB ATTN RDRL CIO MT TECHL PUB ATTN RDRL SER E P AMIRTHARAJ ATTN RDRL SER E F CROWNE ATTN RDRL SER E G BIRDWELL ATTN RDRL SER E P SHAH ATTN RDRL SER E T O'REGAN (5 COPIES) ATTN RDRL SER E R DEL ROSARIO ATTN RDRL SER E T IVANOV ATTN RDRL SER L M CHIN ATTN RDRL SER L M DUBEY ATTN RDRL SER L M ERVIN ADELPHI MD 20783-1197

TOTAL: 29 (27 HCS, 1 ELECT, 1 CD)